molecules

MDPI

Article

Sc@B_{28}^-, Ti@B_{28}, V@B_{28}^+, and V@B_{29}^{2-}: Spherically Aromatic Endohedral Seashell-like Metallo-Borospherenes

Ting Zhang [1,2], Min Zhang [1], Xiao-Qin Lu [3], Qiao-Qiao Yan [1], Xiao-Ni Zhao [1] and Si-Dian Li [1,*]

[1] Institute of Molecular Science, Shanxi University, Taiyuan 030006, China; zhangting0913@sxu.edu.cn (T.Z.); zhangm22@sxu.edu.cn (M.Z.); yanqiaoqiao@sxu.edu.cn (Q.-Q.Y.); zhaoxiaoni@sxu.edu.cn (X.-N.Z.)
[2] Department of Chemistry, Xinzhou Teachers' University, Xinzhou 034000, China
[3] Shanxi Center for Testing of Functional Agro-Products, Shanxi Agricultural University, Taiyuan 030031, China; luxiaoqin@sxu.edu.cn
* Correspondence: lisidian@sxu.edu.cn

Abstract: Transition-metal-doped boron nanoclusters exhibit unique structures and bonding in chemistry. Using the experimentally observed seashell-like borospherenes C_2 $B_{28}^{-/0}$ and C_s B_{29}^- as ligands and based on extensive first-principles theory calculations, we predict herein a series of novel transition-metal-centered endohedral seashell-like metallo-borospherenes C_2 Sc@B_{28}^- (**1**), C_2 Ti@B_{28} (**2**), C_2 V@B_{28}^+ (**3**), and C_s V@B_{29}^{2-} (**4**) which, as the global minima of the complex systems, turn out to be the boron analogues of dibenzenechromium D_{6h} Cr(C_6H_6)$_2$ with two B_{12} ligands on the top and bottom interconnected by four or five corner boron atoms on the waist and one transition-metal "pearl" sandwiched at the center in between. Detailed molecular orbital, adaptive natural density partitioning (AdNDP), and iso−chemical shielding surface (ICSS) analyses indicate that, similar to Cr(C_6H_6)$_2$, these endohedral seashell-like complexes follow the 18-electron rule in bonding patterns ($1S^21P^61D^{10}$), rendering spherical aromaticity and extra stability to the systems.

Keywords: first-principles theory; seashell-like metallo-borospherenes; structures; bonding; spherical aromaticity

Citation: Zhang, T.; Zhang, M.; Lu, X.-Q.; Yan, Q.-Q.; Zhao, X.-N.; Li, S.-D. Sc@B_{28}^-, Ti@B_{28}, V@B_{28}^+, and V@B_{29}^{2-}: Spherically Aromatic Endohedral Seashell-like Metallo-Borospherenes. *Molecules* **2023**, *28*, 3892. https://doi.org/10.3390/molecules28093892

Academic Editor: György Keglevich

Received: 29 March 2023
Revised: 18 April 2023
Accepted: 2 May 2023
Published: 5 May 2023

1. Introduction

Extensive joint photoelectron (PE) spectroscopy and first-principles theory investigations in the past two decades have unveiled a great structural diversity in boron nanoclusters featuring multi-center-two-electron (mc-2e, m ≥ 3) bonding, including the planar or quasi-planar (2D) $B_n^{-/0}$ (n = 3–38, 41, 42) [1–3], cage-like D_{2d} $B_{40}^{-/0}$ and C_3/C_2 B_{39}^- [4,5], and bilayer D_{2h} $B_{48}^{-/0}$[6], with the smallest seashell-like C_2 $B_{28}^{-/0}$ [7] and C_s B_{29}^- [8] observed in gas phases competing with their 2D counterparts in experiments. Based on the experimentally observed cage-like $B_{40}^{-/0}$ and B_{39}^-, the borospherene family have been extended to the B_n^q series (n = 36−42, $q = n - 40$) in theory [9–11]. Theoretical investigations have shown that metal-decorated seashell-like B_{28} may serve as effective potential hydrogen storage materials [12]. The first theoretically predicted perfect cage-like B_{80} in 2007 [13,14] spurred renewed interest in all-boron fullerenes although it was later proved to favor core–shell structures. The bilayer structural motif observed in $B_{48}^{-/0}$ has been extended to B_{48}-B_{72} and B_{84}–B_{98} at the density functional theory (DFT) level, with a bilayer bottom-up approach based on the experimentally observed C_{6v} B_{36} proposed for the observed bilayer BL-α^+ borophenes on Ag (111) [15–19]. Mononuclear core–shell B_{68}, B_{74}, B_{80}, B_{84}, B_{96}, B_{100}, B_{101}, B_{102}, and B_{112} and binuclear core–shell C_s B_{180} ((B_{12})$_2$@B_{156}), C_s B_{182} ((B_{12})$_2$@B_{158}), and C_s B_{184} ((B_{12})$_2$@B_{160}) with two interconnected icosahedral B_{12} cores at the center have also been predicted at DFT, with C_s B_{112} and C_s B_{184} as the most stable mononuclear and binuclear species reported to date in thermodynamics [20–27], respectively. Transition-metal doping proves to induce dramatic structural changes in boron nanoclusters. Perfect transition-metal-centered wheel-like D_{8h} Co©B_8^-, D_{9h} M©B_9^-(M = Rh, Ir, Re), and D_{10h}

M©B_{10}^-(M = Ta, Nb), [28–30] half-sandwich C_{3v} CoB_{12}^- and IrB_{12}^-, and double–ring tubular drum-like D_{8d} CoB_{16}^-, MnB_{16}^-, and RhB_{18}^-, C_s B_2–Ta@B_{18}^-, and D_{10d} Ta@B_{20}^- have been observed in experiments [31–34], with Ta@B_{20}^- possessing the highest coordination number of CN = 20 in tubular species [35]. Perfect lanthanide-metal-doped inverse sandwich D_{nh} $La_2B_n^-$ (n = 7–9) and spherical trihedral metallo-borospherenes $La_3B_{18}^-$ and $Tb_3B_{18}^-$ have also been reported in experiments [36,37]. With inspirations from these experimental observations, our group predicted the smallest core–shell spherical trihedral metallo-boronospherene D_{3h} $La_3[B_2@B_{18}]^-$, perfect spherically aromatic tetrahedral metallo-borospherenes T_d La_4B_{24} and core–shell T_d $La_4B_{29}^{0/+/-}$ ($La_4[B@B_4@B_{24}]^{0/+/-}$), endohedral metallo-borospherenes O_h La_6&$[La@B_{24}]^{+/0}$, and the spherically aromatic trihedral metallo-borospherene D_{3h} La_6B_{30} in a series of recent papers [38–41]. Spherical trihedral metallo-borospherenes and endohedral Complexes of $B_{20}TM_n$ (TM = Sc, Y; n = 3, 4) were predicted recently [42]. The Ta-centered metallo-borospherenes Ta@B_{22}^- and Ta@B_n^q (n = 23–28, q = −1–3) which follow the 18-electron rule, the smallest trihedral metallo-borospherene D_{3h} $Ta_3B_{12}^-$ with three equivalent octacoordinate Ta centers in three η^8–B_8 rings, and spherical tetrahedral metallo–borospherene T_d Ta_4B_{18} with four equivalent nonacoordinate Ta centers in four η^9–B_9 rings conforming to the 18-electron principle were proposed recently [43–46]. Alkaline-earth-metal-centered M@B_{40} (M = Ca, Sr) [47] and actinide-metal-centered U@B_{40} [48] were also predicted in theory. However, to the best of our knowledge, spherically aromatic transition-metal-centered endohedral metallo-borospherenes based on the experimentally observed seashell-like C_2 $B_{28}^{-/0}$ and C_s B_{29}^- as the global minima (GM) of the systems have not been reported in the literature.

As boron analogues of benzene (D_{6h} C_6H_6), the experimentally observed quasi-planar C_{3v} B_{12} with three delocalized π bonds was first utilized as ligands to form the perfect sandwich-like complex D_{3d} $Cr(B_{12})_2$ [49,50]. Unfortunately, such a manually designed complex appears to be a high-lying local minimum of the system unlikely to be produced in experiments. Using the experimentally observed smallest seashell-like borospherenes C_2 $B_{28}^{-/0}$ and C_s B_{29}^- as ligands which contain two B_{12} ligands on the top and bottom interconnected by four or five corner boron atoms on the waist and based on extensive GM searches augmented with first-principles theory calculations, we predict in this work a series of transition-metal-centered seashell-like metallo-borospherenes C_2 Sc@B_{28}^- (**1**), C_2 Ti@B_{28} (**2**), C_2 V@B_{28}^+ (**3**), and C_s V@B_{29}^{2-} (**4**) which, as the GMs of the systems with two interconnected B_{12} ligands on the top and bottom and one transition metal center as the "pearl" sandwiched in between, follow the 18-electron rule in bonding patterns, making the transition-metal-doped boron complexes spherically aromatic in nature, highly stable in both thermodynamics and dynamics and possible to be targeted in future experiments.

2. Results and Discussions

2.1. Structures and Stabilities

The obtained transition-metal-centered seashell-like metallo-borospherenes C_2 Sc@B_{28}^- (**1**), C_2 Ti@B_{28} (**2**), C_2 V@B_{28}^+ (**3**), and C_s V@B_{29}^{2-} (**4**) as the GMs of the systems at PBE0/6-311+G(d) [51], TPSSh/6-311+G(d) [52,53], and CCSD(T)/6-31G(d) [54,55] levels are collectively depicted in Figure 1, with more alternative low-lying isomers summarized in Figures S1–S4 (ESI†). The isovalent Sc@B_{28}^- (1), Ti@B_{28} (2), and V@B_{28}^+ (3) with the calculated coordination energies of E_c = 9.56, 7.83, 7.57 eV and lowest calculated vibration frequencies of 181.13, 186.63, 184.70 cm^{-1} at PBE0, respectively, turn out to have similar seashell-like structures in the same symmetry as their parent C_2 B_{28} ligand [7], with two B_{12} ligands on the top and bottom interconnected by four corner boron atoms on the waist and one transition metal pearl comfortably sandwiched in between. These axially chiral endohedral metallo-borospherene complexes contain a slightly distorted C_2 B_{16} double-ring tube as the basis of the seashell-like structures, two heptagonal windows on the right and left, and thirty-six B_3 triangles on the cage surface, with a transition metal center sandwiched comfortably inside the B_{28} cage along the C_2 molecular axis on the upper end of the B_{16} double-ring tube (see detailed coordination bond lengths tabulated in Table S1). C_2 Sc@B_{28}^-

(1), Ti@B_{28} (2), V@B_{28}^{+} (3) possess the large calculated HOMO-LUMO energy gaps of ΔE_{gap} = 2.10, 2.97, and 3.20 eV at PBE0, respectively, well supporting their high chemical stabilities. It is noticed that the second isomer C_2 Sc&B_{28}^{-} (1b) in Figure S1, an exohedral metallo-borospherene with an octacoordinate Sc atom at the lower end of the B_{16} double-ring tube, is actually iso-energetic with Sc@B_{28}^{-} (1) at CCSD(T), suggesting that the two degenerate C_2 isomers may coexist in experiments, while, as shown in Figures S2 and S3, the endohedral Ti@B_{28} (2) and V@B_{28}^{+} (3) are 0.18 eV and 0.04 eV more stable than their second lowest-lying isomers at CCSD(T), respectively. Triplet and quintet isomers prove to be at least 0.85 eV less stable than their singlet GMs.

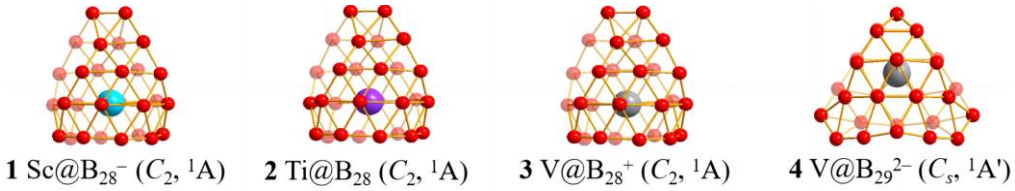

Figure 1. Optimized structures of the transition metal-doped seashell-like endohedral metallo-borospherenes C_2 Sc@B_{28}^{-}(**1**), C_2 Ti@B_{28} (**2**), C_2 V@B_{28}^{+} (**3**), and C_s V@B_{29}^{2-} (**4**) at PBE0/6-311+G(d) level.

The optimized V-centered C_s V@B_{29}^{2-} (**4**) also possesses a seashell-like endohedral structure in the same symmetry as its parent ligand C_s B_{29}^{-} [8]. It contains two B_{12} ligands on the top and bottom interconnected by five corner boron atoms on the waist, two equivalent octagonal windows on the right and left sides, and thirty-eight B_3 triangles on the cage surface, with a vanadium center coordinated inside. With a large calculated HOMO-LUOM energy gap of ΔE_{gap} = 2.39 eV, coordination energy of E_c = 4.79 eV and one small imagery vibrational frequency at −54.30 cm^{-1}, C_s V@B_{29}^{2-}(**4**) appears to be the vibrationally averaged GM of the system between two slightly distorted C_1 V@B_{29}^{2-} isomers (4b in Figure S4) in an a" vibrational mode in which the top B atom and V center swinging left and right reversibly. With zero-point corrections included, C_s V@B_{29}^{2-}(**4**) turns out to be 0.02 eV and 0.06 eV more stable than the second seashell-like isomer C_1 V@B_{29}^{2-} (4b) and third tubular isomer C_s V@B_{29}^{2-} (4c) at CCSD(T), respectively (Figure S4). Triplet and quintet isomers are found to be 0.74 eV and 1.81 eV less stable than singlet C_s V@B_{29}^{2-}(**4**) at PBE0 level, respectively, and all the other isomers lying at least 0.15 eV higher than the C_s GM (**4**).

Detailed natural bonding orbital (NBO) [56] analyses indicate that transition metal centers in Sc@B_{28}^{-} (**1**), Ti@B_{28} (**2**), V@B_{28}^{+} (**3**), and V@B_{29}^{2-} (**4**) possess the net atomic charges 0.76, 0.36, -0.33, and -0.37 |e|, electronic configurations of Sc ([Ar]$4s^{0.19}3d^{1.42}$), Ti ([Ar]$4s^{0.21}3d^{2.02}$), V ([Ar]$4s^{0.22}3d^{4.26}$), and V ([Ar]$4s^{0.20}3d^{4.48}$), and total Wiberger bond orders of 4.03, 6.02, 6.70, and 6.44, respectively. Obviously, transition metal coordination centers in these complexes donate their $4s^2$ electrons almost completely to the boron ligands, while in return, accept partial electrons in their partially filled 4d orbitals from the boron ligands via effective π→3d back-donations, enhancing the thermodynamical stabilities of systems.

Extensive Born–Oppenheimer molecular dynamics (BOMD) [57] simulations on Sc@B_{28}^{-} (**1**) at 600 K, Ti@B_{28} (**2**) at 700 K, and V@B_{29}^{2-} (**4**) at 700 K in Figure S5 clearly indicate that these seashell-like transition metal boron complexes are highly dynamically stable at high temperatures, as evidenced by their small calculated root-mean-square-deviations of RMSD = 0.09, 0.10, 0.10 Å and maximum bond length deviations of MAXD = 0.30, 0.32, 0.33 Å, respectively. No high-lying isomers were observed during the simulations in 30 ps, with the basic structural motifs of the complex systems well maintained in reversible thermal vibrations.

2.2. Bonding Pattern Analyses

To better comprehend the high stabilities of these seashell-like endohedral complexes, detailed adaptive natural density partitioning (AdNDP) [58,59] bonding analyses are performed on Ti@B_{28} (**2**) and V@B_{29}^{2-} (**4**) in Figure 2, in comparison with that of the

prototypic sandwich complex D_{6h} $(C_6H_6)_2Cr$. As indicated in Figure 2a, D_{6h} $(C_6H_6)_2Cr$ possesses 12 2c-2e C-C σ bonds and 12 2c–2e C–H σ bonds on the two C_6H_6 ligands with the occupation numbers ON = 1.95 |e|. Its remaining nine delocalized coordination bonds include 3 7c–2e C_6 (π)–Cr ($d_{\pi/\sigma}$) bonds between the Cr center and C_6H_6 ligand on the top, 3 7c-2e C_6 (π)–Cr ($d_{\pi/\sigma}$) bonds between the Cr center and C_6H_6 ligand at the bottom, and 3 13c C_6 (π)–Cr ($d_{\pi/\sigma}$)–C_6 (π) bonds between Cr center and the two C_6H_6 ligands with ON = 1.93~2.00 |e|, well demonstrating that D_{6h} $(C_6H_6)_2Cr$ satisfies the 18-electron rule.

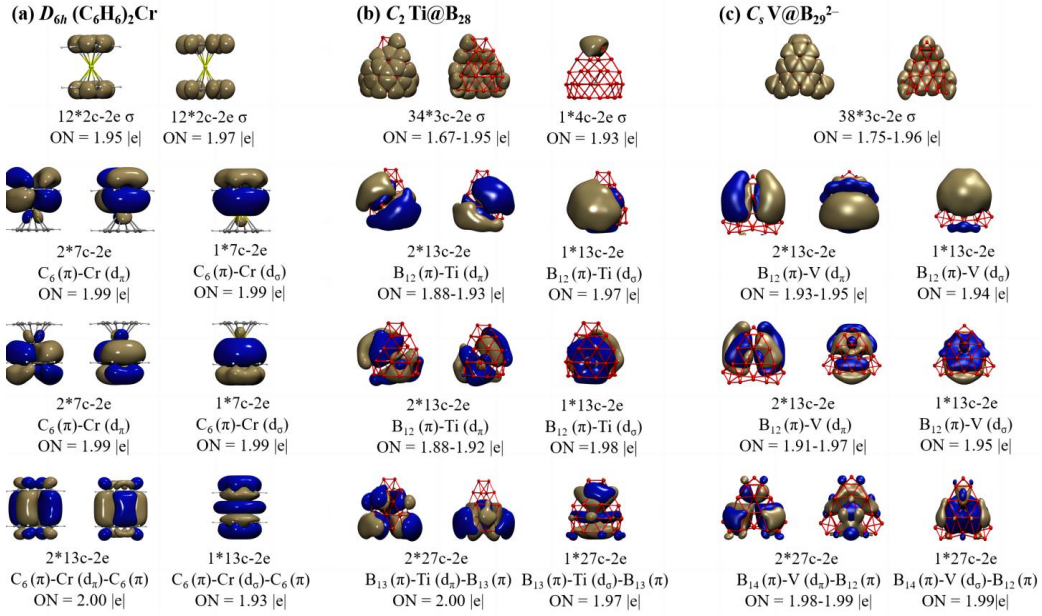

Figure 2. AdNDP bonding patterns of (**a**) D_{6h} $Cr(C_6H_6)_2$, (**b**) C_2 Ti@B_{28} (**2**), and (**c**) C_s V@B_{29}^{2-} (**4**), with the occupation numbers (ON) indicated.

Detailed AdNDP analyses presented in Figure 2b indicate that neutral seashell-like C_2 Ti@B_{28} (**2**) contains 34 3c–2e σ bonds on 34 B_3 triangles on the cage surface and 1 4c–2e σ bond shared by two edge-sharing B_3 triangles on the upper end, forming the σ-framework of the seashell-like complex. Its remaining nine delocalized coordination bonds include three 13c–2e B_{12} (π)–Ti ($d_{\pi/\sigma}$) bonds between the Ti center and B_{12} ligand on the top, three 13c–2e B_{12} (π)–Ti ($d_{\pi/\sigma}$) between the Ti center and B_{12} ligand at the bottom, and three 27c–2e B_{13} (π)–Ti ($d_{\pi/\sigma}$)–B_{13} (π) bonds mainly between Ti and its two B_{12} ligands on the top and bottom with ON = 1.88~2.00 |e|. Such a delocalized coordination bonding pattern possesses a one-to-one correspondence relationship with that of D_{6h} $(C_6H_6)_2Cr$ in Figure 2a, indicating that, similar to $(C_6H_6)_2Cr$, Ti@B_{28} (**2**) follows the 18-electron principle in coordination bonding pattern. Both the isovalent C_2 Sc@B_{28}^- (**1**) and C_2 V@B_{28}^+ (**3**) are found to follow similar bonding patterns (Figure S6).

C_s V@B_{29}^{2-} (**4**) appears to possess a similar bonding pattern. As shown in Figure 2c, it has 38 3c–2e σ bonds on 38 B_3 triangles on the cage surface, forming the σ-framework of the B_{29}^- ligand. The remaining nine delocalized coordination bonds include three 13c–2e B_{12} (π)–V($d_{\pi/\sigma}$) bonds between the V center and B_{12} ligand on the top, three 13c–2e B_{12} (π)–V ($d_{\pi/\sigma}$) between the V center and B_{12} ligand at the bottom, and three 27c–2e B_{14} (π)–V ($d_{\pi/\sigma}$)–B_{12} (π) bonds mainly between V and its two B_{12} ligands on the top and bottom with ON = 1.91~1.99 |e|, again well corresponding to bonding pattern of D_{6h} $(C_6H_6)_2Cr$ in Figure 2a, showing that V@B_{29}^{2-} (**4**) also matches the 18-electron rule in coordination bonding pattern.

The eigenvalue spectra of D_{6h} $(C_6H_6)_2Cr$, C_2 Ti@B_{28} (**2**), and C_s V@B_{29}^{2-} (**4**) compared in Figure S7 indicate that these transition metal-centered complexes possess nine delocalized atomic-like canonical molecular orbitals (CMOs) in the pseudo-superatomic [60] electronic configuration of $1S^21P^61D^{10}$ via effective spd-π interaction/hybridizations, indi-

cating that they follow the 18-electron principle and match the $2(n + 1)^2$ electron counting rule ($n = 2$), making them spherically aromatic in nature and chemically stable both thermodynamically and dynamically.

The calculated iso-chemical shielding surfaces (ICSSs) [61] of $Ti@B_{28}$ (**2**) and $V@B_{29}^{2-}$ (**4**) based on the ZZ components of the calculated nuclear-independent chemical shifts (NICS-ZZ) shown in Figure 3a,c appear to be similar with that of the experimentally known spherically aromatic C_2 B_{28} (Figure 3b) [7] and C_s B_{29}^- (Figure 3d) [8], respectively, well supporting the spherical aromaticity of these endohedral seashell-like endohedral complexes. The spaces inside the boron cage or within 1 Å above the cage surface in vertical directions with negative NICS–ZZ values belong to chemical shielding regions (highlighted in yellow), while the belt-like region outside the cage in the horizontal direction around the waist belongs to the chemical de-shielding area (highlighted in green).

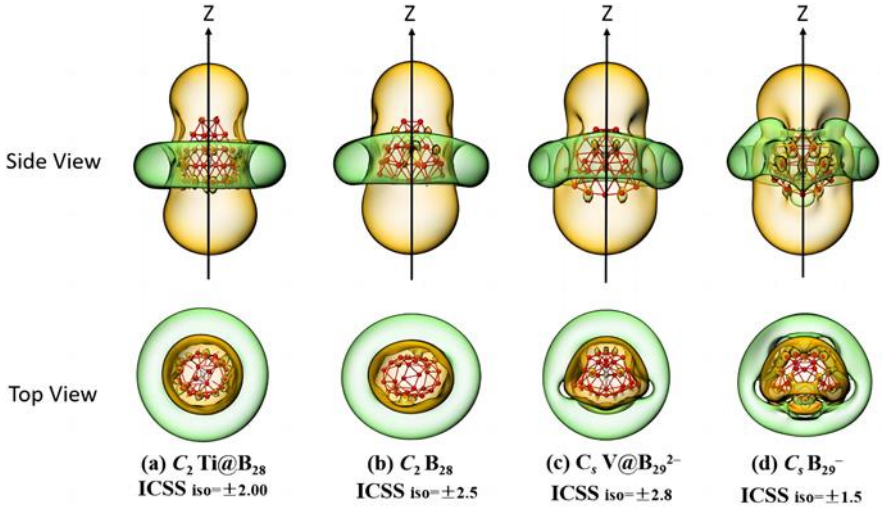

Figure 3. Calculated iso−chemical shielding surfaces (ICSSs) of (**a**) C_2 Ti@B_{28} (**2**) and (**c**) C_s $V@B_{29}^{2-}$ (**4**), compared with that of the experimentally known spherically aromatic (**b**) C_2 B_{28} and (**d**) C_s B_{29}^-, respectively.

2.3. IR, Raman, and PE Spectral Simulations

Joint experimental spectroscopic and first-principles theory investigations have proven to be the most effective method to characterize gas phase clusters [62]. The infrared (IR) and Raman spectra of C_2 $Sc@B_{28}^-$ (**1**), C_2 $Ti@B_{28}$ (**2**), and C_s $V@B_{29}^{2-}$ (**3**) are simulated at PBE0/6-311+G(d) in Figure 4 to facilitate their future spectroscopic characterizations. As shown in Figure 4a, C_2 $Sc@B_{28}^-$ (**1**) exhibits strong IR active peaks at 257 (a), 461 (b), 593 (a), 872 (a), 912 (a), 936 (b), 1030 (a), 1210 (a), and 1365 (a) cm^{-1} which mainly belong to the vibrational modes of the B_{28} skeleton, while its strong Raman active vibrations occur at 181 (a), 258 (b), 411 (a), 515 (a), 621 (a), 1210 cm^{-1} (a), with the 411 cm^{-1} (a) peak corresponding to typical "radial breathing mode" (RBM) [63] of the C_2 B_{28} ligand which can be used to characterize hollow boron nanostructures. The IR and Raman spectra of $Ti@B_{28}$ (Figure 4b) is similar to that of $Sc@B_{28}^-$, with the IR active vibrational modes at 268 (a), 351 (b), 403 (a), 935 (a), 1050 (a), and 1400 (a) and Raman active vibrations at 187 (a), 245 (b), 410 (a), 530 (a), and 631(a) cm^{-1}, respectively, with the 530 cm^{-1} (a) peak belonging to typical RBM. The strong IR peaks of $V@B_{29}^{2-}$ (**4**) occur at 306 (a′), 441 (a′), 572 (a′), 850 (a′), 1022 (a″), 1234 (a″), and 1386 (a″), while its Raman features are located at 253 (a′), 499 (a′), 557 (a′), 648 (a′), 854 (a″), 1100 (a′), and 1373 (a″) (Figure 4c). Simulated IR and Raman spectra of (a) C_2 $V@B_{28}^+$ are shown in Figure S8.

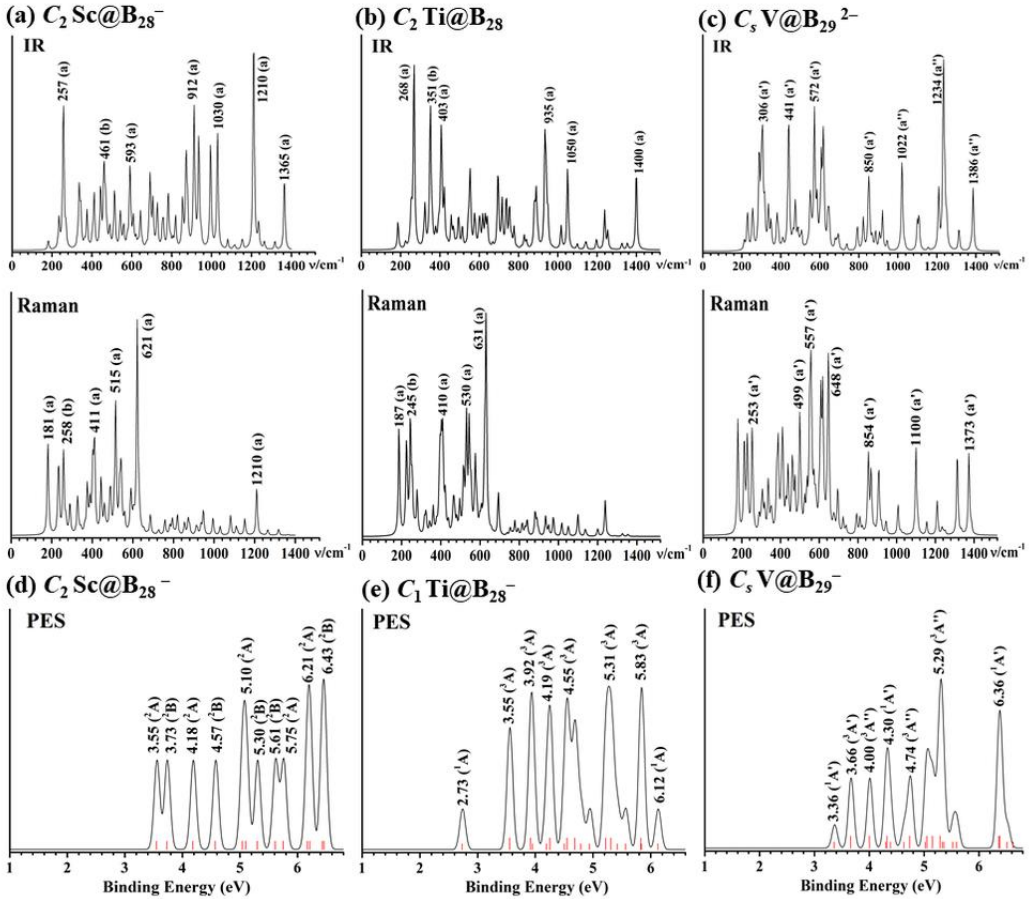

Figure 4. Simulated IR and Raman spectra of (**a**) C_2 Sc@B_{28}^- (**1**), (**b**) C_2 Ti@B_{28} (**2**), and (**c**) C_s V@B_{29}^{2-} (**4**) and PE spectra of (**d**) C_2 Sc@B_{28}^-, (**e**) C_1 Ti@B_{28}^-, and (**f**) C_s V@B_{29}^- at PBE0/6-311+G(d) level. The red bars in (**d**), (**e**,**f**) stand for the positions of calculated PE features, with the long and short red bars in (**e**,**f**) representing triplet and singlet final states in the neutrals, respectively.

The simulated PE spectra of C_2 Sc@B_{28}^- (**1**) and C_1 Ti@B_{28}^- and C_s V@B_{29}^- derived from C_2 Ti@B_{28} (**2**) and C_s V@B_{29}^{2-} (**4**) are shown in Figure 4d–f using the time-dependent TD-PBE0/6-311+G(d) approach [64,65], with their first calculated vertical detachment energies (VDEs) located at 3.55, 2.73, and 3.36 eV and first adiabatic detachment energies (ADEs) located at 3.33, 2.41, and 3.21 eV, respectively. Detachment of one electron from singlet C_2 Sc@B_{28}^- (**1**) leads to doublet final states in its neutral, with the major spectroscopic features at 3.55, 3.73, 4.18, 4.57, 5.10, 5.30, 5.61, 5.75, 6.21, and 6.43 eV, respectively (Figure 4d). Detachment of one electron from the open-shell doublet C_1 Ti@B_{28}^- and C_s V@B_{29}^- generates both singlet or triplet final states in their neutrals, with the major spectral peaks located at 2.73, 3.55, 3.92, 4.19, 4.55, 5.31, 5.83, and 6.12 eV for Ti@B_{28}^- and 3.36 3.66, 4.00, 4.30, 4.74, 5.29, and 6.36 eV for V@B_{29}^-, respectively (Figure 4e,f).

3. Computational Details

Extensive GM searches were performed on Sc@B_{28}^-, Ti@B_{28}, and V@B_{28}^+, V@B_{29}^{2-} at DFT level with electronic multiplicities considered, using both the TGmin2 [66,67] and Minima Hopping (MH) [68,69] codes, in conjunction with manual constructions based on the experimentally observed C_2 $B_{28}^{-/0}$ and C_s B_{29}^- at PBE/DZVP, with about 3500 stationary points probed for each species on its potential surface. The low-lying isomers were then fully optimized at both PBE0/6-311+G(d) [51] and TPSSh/6-311+G(d) [52,53] levels using the Gaussian 09 program, with vibrational frequencies checked to make sure all the obtained low-lying isomers are true minima of the systems. Single point CCSD(T)/6-31G(d) calculations were performed on the five lowest–lying isomers to further

refine their relative energies employing the Molpro (2013) program [54,55], with the T_1 diagnostics checked to make sure that multi-reference interactions make non-significant contributions in these closed-shell complexes. Natural bonding orbital (NBO) analyses were carried out using the NBO 6.0 program [56]. Extensive Born–Oppenheimer molecular dynamics (BOMD) simulations were performed on C_2 $Sc@B_{28}^-$(**1**) at 600 K, C_2 $Ti@B_{28}$ (**2**) at 700 K, and $V@B_{29}^{2-}$(**4**) at 700 K for 30 ps using the CP2K program [57] utilizing the hybrid Gaussian and plane waves method, with the GTH–PBE pseudopotential and DZVP–MOLOPT–SR–GTH basis set for boron and transition metal, respectively. Detailed bonding analyses were carried out utilizing the adaptive natural density partitioning (AdNDP) approach [58,59]. Iso-chemical shielding surfaces (ICSS) [61] were calculated using the Multiwfn 3.8 software [70]. Bonding analyses and ICSS surfaces were visualized using the visual molecular dynamics (VMD) [71] software. The IR and Raman spectra of C_2 $Sc@B_{28}^-$ (**1**), C_2 $Ti@B_{28}$ (**2**), C_s $V@B_{29}^{2-}$ (**4**) were simulated at PBE0/6-311+G(d). The PE spectra of C_2 $Sc@B_{28}^-$ (**1**), C_1 $Ti@B_{28}^-$ and C_s $V@B_{29}^-$ were simulated using the time-dependent DFT approach (TD-DFT) at PBE0/6-311+G(d) level [64,65]. An overall calculation scheme used in this work is presented in Figure S9.

4. Conclusions

Based on the experimentally observed seashell-like C_2 $B_{28}^{-/0}$ and C_s B_{29}^- and extensive first-principles theory calculations, we propose in this work the transition-metal-centered endohedral seashell-like metallo-borospherenes $Sc@B_{28}^-$ (**1**), $Ti@B_{28}$ (**2**), $V@B_{28}^+$ (**3**), and $V@B_{29}^{2-}$ (**4**) which, as the boron analogues to the well-known sandwich complex $Cr(C_2H_6)_2$ highly stable both thermodynamically and dynamically, follow the 18-electron rule in coordination bonding patterns and are spherically aromatic in nature. The IR, Raman, and PE spectra of the concerned species are theoretically simulated to facilitate their future spectroscopic characterizations in gas-phase experiments via laser ablations of boron-transition-metal mixed binary targets. Further combined theoretical and experimental investigations on metal-doped boron complexes are expected to unveil novel structures and bonding in chemistry and materials science and shed new insights on boron-based nano-devices.

Supplementary Materials: The following supporting information can be downloaded at: https://www.mdpi.com/article/10.3390/molecules28093892/s1, Figure S1: Low-lying isomers of C_2 $Sc@B_{28}^-$ with their relative energies; Figure S2: Low-lying isomers of C_2 $Ti@B_{28}$ with their relative energies; Figure S3: Low-lying isomers of C_2 $V@B_{28}^+$ with their relative energies; Figure S4: Low-lying isomers of C_s $V@B_{29}^{2-}$ with their relative energies; Figure S5: Molecular dynamics simulations of (a) $Sc@B_{28}^-$ (1) at 600 K, (b) $Ti@B_{28}$ (2) at 700 K, and (c) $V@B_{29}^{2-}$ (4) at 700 K; Figure S6: AdNDP Analysis of (a) C_2 $Sc@B_{28}^-$ and (b) C_2 $V@B_{28}^+$; Figure S7: Molecular orbital energy levels of (a) D_{6h} $(C_6H_6)_2Cr$, (b) C_2 $Ti@B_{28}$ and (c) C_s $V@B_{29}^{2-}$; Figure S8: Simulated IR and Raman spectra of (a) C_2 $V@B_{28}^+$; Figure S9: An overall scheme of the theoretical procedures adapted in this work. Table S1: The bond lengths r_{Sc-B} of C_2 $Sc@B_{28}^-$, r_{Ti-B} of C_2 $Ti@B_{28}$, r_{V-B} of C_2 $V@B_{28}$ and r'_{V-B} of C_s $V@B_{29}^{2-}$; Table S2: Cartesian coordinates of the optimized low-lying isomers.

Author Contributions: Conceptualization and finalization, S.-D.L.; Validation, T.Z., M.Z., X.-Q.L., Q.-Q.Y. and X.-N.Z.; Writing, T.Z. and S.-D.L. All authors have read and agreed to the published version of the manuscript.

Funding: This work was supported by the National Natural Science Foundation of China (21973057 and 21720102006 to S.-D. L).

Institutional Review Board Statement: Not applicable.

Informed Consent Statement: Not applicable.

Data Availability Statement: Not applicable.

Conflicts of Interest: The authors declare no conflict of interest.

Sample Availability: Samples of the compounds are not available from the authors.

References

1. Jian, T.; Chen, X.-N.; Li, S.-D.; Boldyrev, A.-I.; Li, J.; Wang, L.-S. Probing the structures and bonding of size-selected boron and doped-boron clusters. *Chem. Soc. Rev.* **2019**, *48*, 3550–3591. [CrossRef]
2. Wang, L.-S. Photoelectron spectroscopy of size-selected boron clusters: From planar structures to borophenes and borospherenes. *Int. Rev. Phys. Chem.* **2016**, *35*, 69–142. [CrossRef]
3. Bai, H.; Chen, T.-T.; Chen, Q.; Zhao, X. -Y.; Zhang, Y.-Y.; Chen, W.-J.; Li, W.-L.; Cheung, L.-F.; Bai, B.; Cavanagh, J.; Huang, W.; et al. Planar B_{41}^- and B_{42}^- clusters with double-hexagonal vacancies. *Nanoscale* **2019**, *11*, 23286–23295. [CrossRef] [PubMed]
4. Zhai, H.-J.; Zhao, Y.-F.; Li, W.-L.; Chen, Q.; Bai, H.; Hu, H.-S.; Piazza, Z.-A.; Tian, W.-J.; Lu, H.-G.; Wu, Y.-B.; et al. Observation of an all-boron fullerene. *Nat. Chem.* **2014**, *6*, 727–731. [CrossRef]
5. Chen, Q.; Li, W.-L.; Zhao, Y.-F.; Zhang, S.-Y.; Hu, H.-S.; Bai, H.; Li, H.-R.; Tian, W.-J.; Lu, H.-G.; Zhai, H.-J.; et al. Experimental and theoretical evidence of anaxially chiral borospherene. *ACS Nano.* **2015**, *9*, 754–760. [CrossRef]
6. Chen, W.-J.; Ma, Y.-Y.; Chen, T.-T.; Ao, M.-Z.; Yuan, D.-F.; Chen, Q.; Tian, X.-X.; Mu, Y.-W.; Li, S.-D.; Wang, L.-S. B_{48}^-: A bilayer boron cluster. *Nanoscale* **2021**, *13*, 3868–3876. [CrossRef]
7. Wang, Y.-J.; Zhao, Y.-F.; Li, W.-L.; Jian, T.; Chen, Q.; You, X.R.; Ou, T.; Zhao, X.-Y.; Zhai, H.-J.; Li, S.-D.; et al. Observation and characterization of the smallest borospherene, B_{28}^- and B_{28}. *J. Chem. Phys.* **2016**, *144*, 064307. [CrossRef] [PubMed]
8. Li, H.-R.; Jian, T.; Li, W.-L.; Miao, C.-Q.; Wang, Y.-J.; Chen, Q.; Luo, X.-M.; Wang, K.; Zhai, H.-J.; Li, S.-D.; et al. Competition between quasi-planar and cage-like structures in the B_{29}^- cluster: Photoelectron spectroscopy and ab initio calculations. *Phys. Chem. Chem. Phys.* **2016**, *18*, 29147–29155. [CrossRef]
9. Tian, W.-J.; Chen, Q.; Li, H.-R.; Yan, M.; Mu, Y.-W.; Lu, H.-G.; Zhai, H.-J.; Li, S.-D. Saturn-like charge-transfer complexes $Li_4\&B_{36}$, $Li_5\&B_{36}^+$, and $Li_6\&B_{36}^{2+}$: Exohedral metalloborospherenes with a perfect cage-like B_{36}^{4-} core. *Phys. Chem. Chem. Phys.* **2016**, *18*, 9922–9926. [CrossRef]
10. Liu, H.; Mu, Y.-W.; Li, S.-D. Axially Chiral Cage-like B_{38}^+ and B_{38}^{2+}: New aromatic members of the borospherene family. *J. Cluster Sci.* **2022**, *33*, 81–87. [CrossRef]
11. Chen, Q.; Zhang, S.-Y.; Bai, H.; Tian, W.-J.; Gao, T.; Li, H.-R.; Miao, C.-Q.; Mu, Y.-W.; Lu, H.-G.; Zhai, H.-J.; et al. Cage-like B_{41}^+ and B_{42}^{2+}: New chiral members of the borospherene family. *Angew. Chem. Int. Ed.* **2015**, *54*, 8160–8164. [CrossRef]
12. Si, L.; Tang, C.-M. The reversible hydrogen storage abilities of metal Na (Li, K, Ca, Mg, Sc, Ti, Y) decorated all-boron cage B_{28}. *Int. J. Hydrogen Energ.* **2017**, *42*, 16611–16619. [CrossRef]
13. Szwacki, N.-G.; Sadrzadeh, A.; Yakobson, B.-I. Erratum: B_{80} Fullerene: An ab initio prediction of geometry, stability, and electronic structure. *Phys. Rev. Lett.* **2007**, *98*, 166804. [CrossRef]
14. Research highlights. *Nature* **2007**, *447*, 4–5. [CrossRef]
15. Pei, L.; Yan, Q.-Q.; Li, S.-D. Predicting the structural transition in medium-sized boron nanoclusters: From bilayer B_{64}, B_{66}, B_{68}, B_{70}, and B_{72} to Core-Shell B_{74}. *Eur. J. Inorg. Chem.* **2021**, *2021*, 2618–2624. [CrossRef]
16. Yan, Q.-Q.; Pei, L.; Li, S.-D. Predicting bilayer B_{50}, B_{52}, B_{56} and B_{58}: Structural evolution in bilayer B_{48}–B_{72} clusters. *J. Mol. Model.* **2021**, *27*, 364. [CrossRef]
17. Yan, Q.-Q.; Zhang, T.; Ma, Y.-Y.; Chen, Q.; Mu, Y.-W.; Li, S.-D. A bottom-up approach from medium-sized bilayer boron nanoclusters to bilayer borophene nanomaterials. *Nanoscale* **2022**, *14*, 11443–11451. [CrossRef]
18. Chen, Q.; Wei, G.-F.; Tian, W.-J.; Bai, H.; Liu, Z.-P.; Zhai, H.-J.; Li, S.-D. Quasi-planar aromatic B_{36} and B_{36}^- clusters: All-boron analogues of coronene. *Phys. Chem. Chem. Phys.* **2014**, *16*, 18282–18287. [CrossRef]
19. Ma, Y.-Y.; Zhao, X.-Y.; Zan, W.-Y.; Mu, Y.-W.; Zhang, Z.-H.; Li, S.-D. Prediction of freestanding semiconducting bilayer borophenes. *Nano Res.* **2022**, *15*, 5752–5757. [CrossRef]
20. Prasad, D.-L.; Jemmis, E.-D. Stuffing improves the stability of fullerenelike boron clusters. *Phys. Rev. Lett.* **2008**, *100*, 165504. [CrossRef]
21. Li, H.; Shao, N.; Shang, B.; Yuan, L.-F.; Yang, J.; Zeng, X.C. Icosahedral B_{12}-containing core–shell structures of B_{80}. *Chem. Commun.* **2010**, *46*, 3878–3880. [CrossRef] [PubMed]
22. Zhao, J.-J.; Wang, L.; Li, F.-Y.; Chen, Z.-F. B_{80} and other medium-sized boron clusters: Core−shell structures, not hollow cages. *J. Phys. Chem. A* **2010**, *114*, 9969–9972. [CrossRef] [PubMed]
23. Sai, L.-W.; Wu, X.; Yu, F.-Y. B_{96}: A complete core–shell structure with high symmetry. *Phys. Chem. Chem. Phys.* **2022**, *24*, 15687–15690. [CrossRef]
24. Li, F.-Y.; Jin, P.; Jiang, D.-E.; Wang, L.; Zhang, S.-B.; Zhao, J.-J.; Chen, Z.-F. B_{80} and $B_{101–103}$ clusters: Remarkable stability of the core-shell structures established by validated density functionals. *J. Chem. Phys.* **2012**, *136*, 074302. [CrossRef]
25. Sai, L.-W.; Wu, X.; Gao, N.; Zhao, J.-J.; King, R.-B. Boron clusters with 46, 48, and 50 atoms: Competition among the core–shell, bilayer and quasi-planar structures. *Nanoscale* **2017**, *9*, 13905–13909. [CrossRef] [PubMed]
26. Zhang, M.; Lu, H.-G.; Li, S.-D. B_{111}, B_{112}, B_{113}, and B_{114}: The most stable core-shell borospherenes with an icosahedral B_{12} core at the center exhibiting superatomic behaviors. *Nano Res.* **2021**, *14*, 4719–4724. [CrossRef]
27. Zhang, M.; Jia, W.-P.; Zhang, T.; Pei, B.-B.; Xu, J.; Tian, X.-X.; Lu, H.-G.; Li, S.-D. Superatomic icosahedral-C_nB_{12-n} (n = 0, 1, 2) stuffed mononuclear and binuclear borafullerene and borospherene nanoclusters with spherical aromaticity. *Sci. Rep.* **2022**, *12*, 19741. [CrossRef]
28. Romanescu, C.; Galeev, T.-R.; Li, W.-L.; Boldyrev, A.-I.; Wang, L.-S. Aromatic metal-centered monocyclic boron rings: $Co©B_8^-$ and $Ru©B_9^-$. *Angew. Chem.* **2011**, *50*, 9334–9337. [CrossRef]

29. Chen, T.-T.; Li, W.-L.; Bai, H.; Chen, W.-J.; Dong, X.-R.; Li, J.; Wang, L.-S. Re©B_8^- and Re©B_9^-: New members of the transition-metal-centered borometallic molecular wheel family. *J.Phys. Chem. A* **2019**, *123*, 5317–5324. [CrossRef]
30. Romanescu, C.; Galeev, T.-R.; Li, W.-L.; Boldyrev, A.-I.; Wang, L.-S. Transition-metal-centered monocyclic boron wheel clusters (M©B_n): A new class of aromatic borometallic compounds. *Acc. Chem. Res.* **2013**, *46*, 350–358. [CrossRef]
31. Popov, I.-A.; Li, W.-L.; Piazza, Z.-A.; Boldyrev, A.-I.; Wang, L.-S. Complexes between planar boron clusters and transition metals: A photoelectron spectroscopy and ab initio study of CoB_{12}^- and RhB_{12}^-. *J. Phys. Chem. A* **2014**, *118*, 8098–8105. [CrossRef] [PubMed]
32. Popov, I.-A.; Jian, T.; Lopez, G.-V.; Boldyrev, A.-I.; Wang, L.-S. Cobalt-centred boron molecular drums with the highest coordination number in the CoB_{16}^- cluster. *Nat. Commun.* **2015**, *6*, 8654. [CrossRef] [PubMed]
33. Jian, T.; Li, W.-L.; Popo, I.-A.; Lope, G.-V.; Chen, X.; Boldyrev, A.-I.; Li, J.; Wang, L.-S. Manganese-centered tubular boron cluster–MnB_{16}^-: A new class of transition-metal molecules. *J. Chem. Phys.* **2016**, *144*, 154310. [CrossRef]
34. Jian, T.; Li, W.-L.; Chen, X.; Chen, T.-T.; Lopez, G.-V.; Li, J.; Wang, L.S. Competition between drum and quasi-planar structures in RhB_{18}^-: Motifs for metallo-boronanotubes and metallo-borophenes. *Chem. Sci.* **2016**, *7*, 7020–7027. [CrossRef]
35. Li, W.-L.; Jian, T.; Chen, X.; Li, H.-R.; Chen, T.-T.; Luo, X.-M.; Li, S.-D.; Li, J.; Wang, L.-S. Observation of a metal-centered B_2-Ta@B_{18}^- tubular molecular rotor and a perfect Ta@B_{20}^- boron drum with the record coordination number of twenty. *Chem. Commun.* **2017**, *53*, 1587–1590. [CrossRef] [PubMed]
36. Chen, T.-T.; Li, W.-L.; Li, J.; Wang, L.-S. [La(η^x-B_x)La]$^-$ (x = 7–9): A new class of inverse sandwich complexes. *Chem. Sci.* **2019**, *10*, 2534–2542. [CrossRef]
37. Chen, T.-T.; Li, W.-L.; Chen, W.-J.; Yu, X.-H.; Dong, X.-R.; Li, J.; Wang, L.-S. Spherical trihedral metallo-borospherenes. *Nat. Commun.* **2020**, *11*, 2766. [CrossRef] [PubMed]
38. Zhao, X.-Y.; Yan, M.; Wei, Z.-H.; Li, S.-D. Donor–acceptor duality of the transition-metal-like B_2 core in core–shell-like metallo-borospherenes La_3&[B_2@B_{17}]$^-$ and La3&[B_2@B_{18}]$^-$. *RSC Adv.* **2020**, *10*, 34225–34230. [CrossRef]
39. Lu, X.-Q.; Gao, C.-Y.; Wei, Z.-H.; Li, S.-D. Cage-like La_4B_{24} and Core-Shell $La_4B_{29}^{0/+/-}$: Perfect spherically aromatic tetrahedral metallo-borospherenes. *J. Mol. Model.* **2021**, *27*, 130. [CrossRef]
40. Lu, X.-Q.; Ao, M.-Z.; Tian, X.-X.; Zan, W.-Y.; Mu, Y.-W.; Li, S.-D. Perfect cubic La-doped boron clusters La_6&[La@B_{24}]$^{+/0}$ as the embryos of low-dimensional lanthanide boride nanomaterials. *RSC Adv.* **2020**, *10*, 12469–12474. [CrossRef]
41. Ao, M.-Z.; Lu, X.-Q.; Mu, Y.-W.; Zan, W.-Y.; Li, S.-D. La@[La_5&B_{30}]$^{0/-/2-}$: Endohedral trihedral metallo-borospherenes with spherical aromaticity. *Phys. Chem. Chem. Phys.* **2022**, *24*, 3918–3923. [CrossRef]
42. Yan, L.-J. Large B_7 triangles in hollow spherical trihedral metallo-borospherenes and their endohedral complexes of $B_{20}TM_n$ (TM = Sc, Y; n = 3, 4): A theoretical characterization. *Inorg. Chem.* **2022**, *61*, 10652–10660. [CrossRef]
43. Li, H.-R.; Liu, H.; Lu, X.-Q.; Zan, W.-Y.; Tian, X.-X.; Lu, H.-G.; Wu, Y.-B.; Mu, Y.-W.; Li, S.-D. Cage-like Ta@B_n^q complexes (n = 23–28, q = −1– +3) in 18-electron configurations with the highest coordination number of twenty-eight. *Nanoscale* **2018**, *10*, 7451–7456. [CrossRef]
44. Li, H.-R.; Liu, H.; Tian, X.-X.; Zan, W.-Y.; Mu, Y.-W.; Lu, H.-G.; Li, J.; Wang, Y.-K.; Li, S.-D. Structural transition in metal-centered boron clusters: From tubular molecular rotors Ta@B_{21} and Ta@B_{22}^+ to cage-like endohedral metalloborospherene Ta@B_{22}^-. *Phys. Chem. Chem. Phys.* **2017**, *19*, 27025–27030. [CrossRef] [PubMed]
45. Zhang, Y.; Zhao, X.-Y.; Yan, M.; Li, S.-D. From inverse sandwich $Ta_2B_7^+$ and Ta_2B_8 to spherical trihedral $Ta_3B_{12}^-$: Prediction of the smallest metallo-borospherene. *RSC. Adv.* **2020**, *10*, 29320–29325. [CrossRef] [PubMed]
46. Zhang, Y.; Lu, X.-Q.; Yan, M.; Li, S.-D. Perfect spherical tetrahedral metallo-borospherene Ta_4B_{18} as a superatom following the 18-electron rule. *ACS Omega* **2021**, *6*, 10991–10996. [CrossRef] [PubMed]
47. Bai, H.; Chen, Q.; Zhai, H.-J.; Li, S.-D. Endohedral and exohedral metalloborospherenes: M@B_{40} (M=Ca, Sr) and M&B_{40} (M=Be, Mg). *Angew Chem Int Ed.* **2015**, *54*, 941–945. [CrossRef]
48. Yu, T.-R.; Gao, Y.; Xu, D.-X.; Wang, Z.-G. Actinide endohedral boron clusters: A closed-shell electronic structure of U@B_{40}. *Nano Res.* **2018**, *11*, 354–359. [CrossRef]
49. Czekner, J.; Cheung, L.-F.; Wang, L.-S. Probing the structures of neutral B_{11} and B_{12} using high-resolutionphotoelectron imaging of B_{11}^- and B_{12}^-. *J. Phys. Chem. C.* **2017**, *121*, 10752–10759. [CrossRef]
50. Yuan, Y.; Cheng, L.-J. Ferrocene analogues of sandwich B_{12}·Cr·B_{12}: A theoretical study. *J. Chem. Phys.* **2013**, *138*, 024301. [CrossRef]
51. Adamo, C.; Barone, V. Toward reliable density functional methods without adjustable parameters: The PBE0 model. *J. Chem. Phys.* **1999**, *110*, 6158–6170. [CrossRef]
52. Staroverov, V.-N.; Scuseria, G.-E.; Tao, J.; Perdew, J.-P. Comparative assessment of a new nonempirical density functional: Molecules and hydrogen-bonded complexes. *J. Chem. Phys.* **2003**, *119*, 12129–12137. [CrossRef]
53. Krishnan, R.; Binkley, J.-S.; Seeger, R.-J.; Pople, A. Self-consistent molecular orbital methods. XX. A basis set for correlated wave functions. *J. Chem. Phys.* **1980**, *72*, 650–654. [CrossRef]
54. Purvis, G.-D., III; Bartlett, R.-J. A full coupled-cluster singles and doubles model: The inclusion of disconnected triples. *J. Chem. Phys.* **1982**, *76*, 1910–1918. [CrossRef]
55. Raghavachari, K.; Trucks, G.-W.; Pople, J.-A.; Head-Gordon, M. A fifth-order perturbation comparison of electron correlation theories. *Chem. Phys. Lett.* **1989**, *157*, 479–483. [CrossRef]
56. Glendening, E.-D.; Landis, C.-R.; Weinhold, F. NBO 6.0: Natural bond orbital analysis program. *J. Comput. Chem.* **2013**, *34*, 1429–1437. [CrossRef] [PubMed]

57. Vondele, J.-V.; Krack, M.; Mohamed, F.; Parrinello, M.; Chassaing, T.-S.; Hutter, J. Quickstep: Fast and accurate density functional calculations using a mixed Gaussian and plane waves approach. *Comput. Phys. Commun.* **2005**, *167*, 103–128. [CrossRef]
58. Zubarev, D.-Y.; Boldyrev, A.-I. Developing paradigms of chemical bonding: Adaptive natural density partitioning. *Phys. Chem. Chem. Phys.* **2008**, *10*, 5207–5217. [CrossRef] [PubMed]
59. Tkachenko, N.-V.; Boldyrev, A.-I. Chemical bonding analysis of excited states using the adaptive natural density partitioning method. *Phys. Chem. Chem. Phys.* **2019**, *21*, 9590–9596. [CrossRef] [PubMed]
60. Kang, S.-Y.; Nan, Z.-A.; Wang, Q.-M. Superatomic orbital splitting in coinage metal nanoclusters. *J. Phys. Chem. Lett.* **2022**, *13*, 291–295. [CrossRef] [PubMed]
61. Kleinpeter, E.; Klod, S.; Koch, A. Visualization of through space NMR shieldings of aromatic and anti-aromatic molecules and a simple means to compare and estimate aromaticity. *J. Mol. Struc: Theochem.* **2007**, *811*, 45–60. [CrossRef]
62. Wang, G.-J.; Zhou, M.-F.; Goettel, J.-T.; Schrobilgen, G.-J.; Su, J.; Li, J.; Schloeder, T.; Riedel, S. Identification of an iridium-containing compound with a formal oxidation state of IX. *Nature* **2014**, *514*, 475–477. [CrossRef]
63. Ciuparu, D.; Klie, R.-F.; Zhu, Y.-M.; Pfefferle, L. Synthesis of pure boron single-wall nanotubes. *J. Phys. Chem. B.* **2004**, *108*, 3967–3969. [CrossRef]
64. Bauernschmitt, R.; Ahlrichs, R. Treatment of electronic excitations within the adiabatic approximation of time dependent density functional theory. *Chem. Phys. Lett.* **1996**, *256*, 454–464. [CrossRef]
65. Casida, M.-E.; Jamorski, C.; Casida, K.-C.; Salahub, D.-R. Molecular excitation energies to high-lying bound states from time-dependent density-functional response theory: Characterization and correction of the time-dependent local density approximation ionization threshold. *J. Chem. Phys.* **1998**, *108*, 4439–4449. [CrossRef]
66. Zhao, Y.-F.; Chen, X.; Li, J. TGMin: A global-minimum structure search program based on a constrained basin-hopping algorithm. *Nano Res.* **2017**, *10*, 3407–3420. [CrossRef]
67. Chen, X.; Zhao, Y.-F.; Zhang, Y.-Y.; Li, J. TGMin: An efficient global minimum searching program for free and surface-supported clusters. *J. Comput. Chem.* **2019**, *40*, 1105–1112. [CrossRef]
68. Goedecker, S. Minima hopping: An efficient search method for the global minimum of the potential energy surface of complex molecular systems. *J. Chem. Phys.* **2004**, *120*, 9911–9917. [CrossRef]
69. Goedecker, S.; Hellmann, W.; Lenosky, T. Global Minimum Determination of the Born-Oppenheimer Surface within Density Functional Theory. *Phys. Rev. Lett.* **2005**, *95*, 055501. [CrossRef]
70. Lu, T.; Chen, F.-W. Multiwfn: A multifunctional wavefunction analyzer. *J. Comput. Chem.* **2012**, *33*, 580–592. [CrossRef]
71. Humphrey, W.; Dalke, A.; Schulten, K. VMD: Visual molecular dynamics. *J. Mol. Graphics.* **1996**, *14*, 33. [CrossRef] [PubMed]